



Functionalizing Cu nanoparticles with fluoric polymer to enhance C₂₊ product selectivity in membraned CO₂ reduction

Tete Zhao ^{a,b}, Xupeng Zong ^c, Jiuding Liu ^a, Jialei Chen ^a, Keqiang Xu ^a, Xiao Wang ^a, Xijie Chen ^a, Wutong Yang ^a, Fangming Liu ^a, Meng Yu ^{a,*}, Fangyi Cheng ^{a,b,**}

^a Key Laboratory of Advanced Energy Materials Chemistry (Ministry of Education), Engineering Research Center of High-efficiency Energy Storage (Ministry of Education), College of Chemistry, Nankai University, Tianjin 300071, China

^b Haihe Laboratory of Sustainable Chemical Transformations, Tianjin 300192, China

^c Dalian Institute of Chemical Physics, Chinese Academy of Sciences, Dalian 116023, China



ARTICLE INFO

Keywords:

CO₂ reduction
Hydrophobic layer
Cu catalyst
Polymer coating
Membrane electrode assembly electrolyzer

ABSTRACT

Copper-based nanomaterials are attractive in CO₂ electroreduction into valuable chemicals but still suffer from limited selectivity of C₂₊ products due to the parasitic hydrogen evolution reaction and inefficient dimerization of absorbed CO intermediate (*CO). Herein, we report an *in situ* polymerization strategy to coat hydrophobic polymer containing methoxyl silane ((CH₃O)₃Si-) and trifluoromethyl (-CF₃) functional groups on Cu nanoparticles. The optimized Cu-poly exhibits a high Faradaic efficiency of 71.08 % and a remarkable partial current density of 355.4 mA cm⁻² for C₂₊ products in a membrane electrode assembly electrolyzer using a bicarbonate electrolyte. A combined study of density functional theory calculations and *in situ* infrared characterizations indicates that the enhanced performances could be ascribed to the decreased formation energy of *COCOH, induced by the withdraw-electron effect of -CF₃ and enhanced coverage of *CO. This work offers a new insight in tuning the electrocatalytic microenvironment through the surface polymerization process.

1. Introduction

Electrochemical CO₂ reduction reaction (CO₂RR) to value-added fuels and chemicals from clean electricity generated by renewable sources such as wind and solar is an attractive way of energy storage and conversion [1,2]. Among various metals (e.g., Ag, Au, Sn, Cu, etc.) explored so far, Cu is the only metal that can balance the adsorption of *CO and *H intermediates due to its unique electronic properties, thus strongly reducing CO₂ into C₂₊ products including ethylene (C₂H₄), ethanol (EtOH), and propanol (PrOH) [3–6]. However, the competitive hydrogen evolution reaction (HER) and weak *CO dimerization in aqueous electrolytes still limit the dimerization process and thus the formation of C₂₊ products [7]. To date, tremendous efforts have been devoted to tailoring the catalytic activity of Cu-based catalysts in CO₂RR, such as morphology [8,9], facets [10–12], oxidation state [13, 14], particle size [15,16], and so on. Among them, modification of the catalytic microenvironment is of particular interest in tuning local pH and the concentration of intermediates, which can promote

electrode/electrolyte performances for enhanced C₂₊ selectivity [17–21].

In addition to the selectivity, the partial current density of C₂₊ products on Cu is also an important factor for practical CO₂RR applications. The low solubility of CO₂ in water (35 mM at 298 K and 1 atm pressure) and the thick diffusion layer of CO₂ mass transfer make it difficult in H-type cell to meet industrial current requirements [22,23]. Previous studies have shown that zero-gap membrane assembly electrodes (MEA) can achieve ampere-scale current densities, benefiting from the reduced mass transfer resistance and diffusion pathway of gaseous CO₂ [24,25]. Although the catholyte-free design greatly alleviates the formation of carbonate precipitates in neutral or alkaline electrolytes as compared to flow cell, parasitic HER and unexpected salt precipitates exist in MEA configurations due to two factors. Firstly, the CO₂RR is a proton-consumption reaction that can create a strongly alkaline microenvironment, which induces to form hydroxide deposits. Secondly, cations from anolyte can pass through the anion-exchange membrane to react with local hydroxyls under the driving force of an

* Corresponding author.

** Corresponding author at: Key Laboratory of Advanced Energy Materials Chemistry (Ministry of Education), Engineering Research Center of High-efficiency Energy Storage (Ministry of Education), College of Chemistry, Nankai University, Tianjin 300071, China.

E-mail addresses: mengyu@nankai.edu.cn (M. Yu), fycheng@nankai.edu.cn (F. Cheng).

applied electric field [26]. Moreover, the formation of salt precipitates can reduce the CO₂ utilization and overall energy efficiency of MEA devices. Thus, the management of water and salt in MEA electrolyzer is desirable. Of particular note, tuning interfacial water on the surface of gas diffusion layer (GDL) is the focus to solving the problem of competitive HER and salt formation. Furthermore, water can also affect the distribution of products on the gas diffusion electrode (GDE) [27, 28]. Introducing hydrophobic nanoparticles into the catalysts layer and coating the catalyst surface with hydrophobic organic molecules have proven effective to improve the hydrophobicity of GDL [29–33]. In spite of substantial progress, it remains challenging to simultaneously control the hydrophobicity and surface oxidation state of Cu-based catalysts.

In this work, we report a hydrophobic modification catalyst consisting of Cu nanoparticles and fluoroc polymers (Cu-poly), which serves as an efficient catalyst for catalyzing CO₂ into C₂₊ products. A combined experimental/computational study demonstrates that the fluoroc polymers functionalized Cu-poly enhances the coverage of *CO species and decreases the formation energy of the key intermediates (*COCOH) by the hydrogen bond. As a result, the prepared Cu-poly catalysts shows an improved Faradaic efficiency (FE) of 71.08 % for C₂₊ hydrocarbons at –3.98 V, as compared to bare Cu (FE_{C2+} 61.59 %). This work proposes a facile surface polymerization pathway to tune the electrocatalytic microenvironment in the reduction of CO₂ to C₂₊ products and would provide new insight into addressing the selectivity challenges in practical CO₂RR at industrial scale.

2. Experimental section

2.1. Chemical reagents

All chemicals and reagents were purchased from commercial sources and used without further treatment. Cu nanoparticles (Cu 99.5 %) were purchased from Sigma-Aldrich (Shanghai) Trading. N,N-dimethylacetamide (DMAc, AR, 99.0 %) and absolute ethanol (99.5 %) were purchased from the Shanghai Aladdin Biochemical Technology. 2,2,2-trifluoroethyl methacrylate (TFEMA, 98.0 %) and 3-methacryloxypropyltrimethoxysilane (MAPTMS, 97.0 %) were purchased from Anhui Senrise Technology. 2,2-azobis (2-methylpropionitrile) (AIBN, 98.0 %) and deuterium oxide (D₂O, 99.9 %) were purchased from Adamas-Beta (Shanghai) Chemical Reagent. Dimethyl sulfoxide (DMSO, 99.0 %) and potassium bicarbonate (KHCO₃, ≥99.99 %) were obtained from Shanghai Macklin Biochemical. Ferric nitrate nonahydrate (Fe(NO₃)₃•9 H₂O, 98.0 %) was purchased from the Xiya Chemical Technology (Shangdong). Nafion D-521 dispersion (5 % W/W in water and 1-propanol, exchange capacity ≥ 0.92 meq/g) was bought from Alfa Aesar China Chemical. Ni foam was purchased from Tianjin Eilian Electronics & Technology. Anion-exchange membrane (AEM, X37-Grade 50 RT) and the GDL (YLS-30 T), which consists of a carbon fiber paper and a microporous layer surface coating with poly (tetrafluoroethylene) (PTFE) hydrophobic treatment, were purchased from Dioxide Materials. All the electrolytes were prepared using ultrapure water (18.2 MΩ cm⁻¹).

2.2. Synthesis of polymer modified Cu NPs

Cu-poly-1 was prepared by following previous report with a slight modification [34]. Briefly, 100.0 mg Cu NPs were ultrasonically dispersed in 20.0 mL of DMAc for 5 min. Then 87.0 μL MAPTMS and 750.0 μL TFEMA were rapidly added to the above dark solution and ultrasonication for another 30 min. After that, 6.0 mg AIBN was added to the above suspension, and the reactor was placed in an oven at 75 °C for 4 h. The dark catalyst was then collected by centrifugation and washed three times with ethanol and dried in a vacuum oven at 80 °C overnight. Cu-poly-2 was prepared with similar procedures, except that the additive amounts of MAPTMS and AIBN were increased to 325.0 μL and 20.0 mg, respectively.

2.3. Characterizations

The crystal phase was identified by powder X-ray diffraction (XRD, MimFlex600, Rigaku, Japan) spectroscopy with Cu Kα radiation (40 kV, λ = 1.5406 Å and 15 mA) at a scan rate of 10 min⁻¹ with the 2-Theta degree from 5° to 85°. The composition, microstructure and morphology were investigated on Raman spectroscopy (InVia Reflex, Renishaw, UK), Fourier transform infrared (FTIR) reflection spectroscopy (Nicolet iS50, Thermo Fisher Scientific, USA), field emission scanning electron microscopy (SEM, JSM-7900F, JEOL, Japan) at an accelerating voltage of 1.0 kV, and high-resolution transmission electron microscopy (HRTEM, Talos F200X G2, FEI Czech Republic) equipped with energy dispersive X-ray spectroscopy (EDS). Nitrogen and carbon dioxide adsorption/desorption measurements were conducted on a Micromeritics ASAP 2460 Analyzer (USA). Pore volumes and pore sizes were calculated by the pore-size distribution curves from the desorption isotherms using the density functional theory (DFT) methods. The valence states of samples were analyzed using X-ray photoelectron spectroscopy (XPS, Axis Ultra DLD, Kratos Analytical Ltd, UK). Aberration-corrected high-angle annular dark-field scanning transmission electron microscopy (AC-HAADF-STEM) images were collected on JEOL JEM-ARM200F NEOARM equipped with aberration corrector for STEM. The microscope was operated at 200 kV. Elemental analysis was performed on elemental analyzer (vario EL CUBE, elementar, Germany).

2.4. Preparation of cathode and anode

GDL: GDL serves as a cathodic catalyst support and consists of hydrophobic macroporous carbon nanofibers (Fig. S1a) with hydrophobicity and high gas permeability, and conducting carbon black (Fig. S1b).

Cathode preparation: For CO₂RR cathode preparation, 60.0 mg catalysts and 60.0 μL Nafion solution were mixed in 3.0 mL ethanol and sonicated for 1 h to prepare catalyst ink. The prepared ink was sprayed on 2.89 cm² of hydrophobic GDL and the loading of the catalyst was adjusted to ~1.0 mg cm⁻².

Anode preparation: According to previous report, nickel iron layered double hydroxide (NiFe LDH) was synthesized by wet chemical etching with a slight modification [35]. Typically, a piece of Ni foam (1.9 × 1.9 cm) was pre-cleaned with 5 wt% HCl for 1 h under ultrasonication and then washed by deionized water and ethanol. After that, 60.0 mg Fe (NO₃)₃•9 H₂O was dissolved in 20.0 mL H₂O and sonicated for another 30 min. Then, Ni foam was immersed in the above dark red solution and left overnight at room temperature. After treatment, the as-obtained foam was rinsed with water and ethanol for several times to remove residual salts. The treated Ni foam was then dried in an oven at 80 °C overnight for further use.

Pretreatment of AEM: X37-Grade 50 RT membranes were activated in 1 M KOH for 12 h at room temperature and washed three times with ultrapure water before use.

2.5. Electrochemical measurements and products qualification

MEA measurements: CO₂RR measurements were carried out in an MEA electrolyzer (purchased from Suzhou Sinero Technology) equipped with domestic titanium plate electroplated with Au film, which is used as the current collector. The cell consists of anode (NiFe LDH), silicone gasket, AEM and catalysts cathode, and is bolted to prevent gas or liquid leakage or crossover. The pressure of the cell was first stabilized before each electrochemical test. Typically, CO₂ was humidified by bubbling through a glass bottle contained 30.0 mL of water at room temperature and flowed to the cathode of the cell with a gas flow rate of 60.0 mL min⁻¹. For the anode, 40.0 mL anolyte of 1 M KHCO₃ was cycled by a peristaltic pump with a flow rate of 6.0 mL min⁻¹. A sealed glass vial with 20.0 mL of water in cold trap was used to collect liquid products

such as ethanol, propanol, formate, and acetate [36]. All CO₂RR electrochemical data were collected using a P4000 electrochemical workstation (Solartron, PAR-Ametek). Gas products were simultaneously analyzed every 11 min using an online gas chromatograph (GC, Shimadzu 2014 C). The GC was equipped with a flame ionization detector (FID) for quantification of CH₄, C₂H₄, and CO and a thermal conductivity detector (TCD) for H₂, using Ar as the carrier gas. Liquid products were quantified by ¹H NMR spectroscopy on a 400 MHz spectrometer (Quantum-1, Zhongke-Niujin MR Tech). To record NMR data, 20.0 mL of catholyte from the cold trap was collected and 40.0 mL of anolyte was mixed for further use. A 30.0 mL of electrolyte was taken out from the mixture and then 20.0 μL DMSO was added as an internal standard. Finally, 450.0 μL of the above solution and 50.0 μL D₂O were transferred to a sample tube and analyzed on NMR spectrometer. The water peak in each spectrum was suppressed using previous method [37]. Faradaic efficiencies were calculated according to the equation [4]:

$$FE_x(\%) = \frac{n_x \times n_{ex}^- \times F}{Q} \times 100$$

where n_x is the amount (mol) of product x , n_{ex}^- is the number of electron to form x from CO₂/H₂O, F is the Faraday constant (94685 C mol⁻¹), and Q is the charge passed to generate n_x .

The products formation rate (r , μmol cm⁻² h⁻¹), which represents the quantity of all products obtained per unit of area and time [38], is calculated by the following equation [39]:

$$\text{Formation rate} = (Q_{\text{tot}} \times FE_x) / (96,485 \times n_x \times t \times S)$$

where Q_{tot} is the total charge, t is the electrolysis time (h), S is the geometric area of the cathode (cm²), and n_x is the molar amount of the products.

2.6. In situ infrared spectroscopy

Attenuated total reflection surface-enhanced infrared spectroscopy (ATR-SEIRAS) was conducted using a FTIR spectrometer (Nicolet iS50, Thermo Fisher Scientific, USA) equipped with a Mercury Cadmium Telluride (MCT) detector, which was cooled with liquid nitrogen. The ATR-SEIRAS spectra were recorded at a resolution of 4.0 cm⁻¹ and a range of 400–4000 cm⁻¹, with 32 interferograms collected for each spectrum. Electrochemical measurements were performed using a three-electrode measurement system with Pt foil as the counter electrode and Ag/AgCl as the reference electrode. Fig. S2 illustrates the configuration and digital photograph of in situ ATR-SEIRAS cell. Firstly, Au films were prepared by sputtering Au NPs onto the surface of the Si prism, which plays a key role in enhancing the signal of intermediate species [40]. Then, the catalyst ink containing Cu NPs or Cu-poly catalyst was dropped on the surface of the Au film to form the working electrode. Real-time FTIR spectra were recorded during the chronopotentiometry tests with operating potentials from the open circuit potential to −1.4 V (vs. RHE) in CO₂-saturated 1 M KHCO₃ solution. The increment of applied potentials was 100.0 mV and the test time was 80.0 s

2.7. Calculation methods and models

DFT calculations were performed by Vienna ab initio simulation package (VASP) using the generalized gradient approximation with the Perdew–Burke–Ernzerhof exchange-correlation functional (GGA-PBE) for describing the interactions in the absence of magnetic moments [41, 42]. Van der Waals interactions were included using the DFT+D3 approach developed by Grimme, with zero damping. The electronic iterations convergence was set to 1×10^{-6} eV using the Fast (Davidson and RMM-DIIS) algorithm and reciprocal space projection operators. The planewave cutoff energy was set to 400.0 eV with a $1 \times 1 \times 1$ mesh and k-spacing of 0.5 per Angstrom. The k-mesh was centered on the gamma point. First-order Methfessel-Paxton smearing with a width of

0.2 eV was employed in the calculations. The accuracy of calculations was verified by ensuring that the convergence criteria were met. We used a 6×6 four-layer periodic model of Cu (111) to simulate the surface, and 15 Å was selected as the vacuum layer [43]. In the model, surface relaxation was considered. Only the top two layers were permitted to relax during the optimization stage. While the bottom two levels were fixed, the top two layers were movable. A trimer is composed of three types of monomers, which is used to simplify the simulation of high molecular copolymer and is placed on the surface of Cu for adsorption calculation.

3. Results and discussion

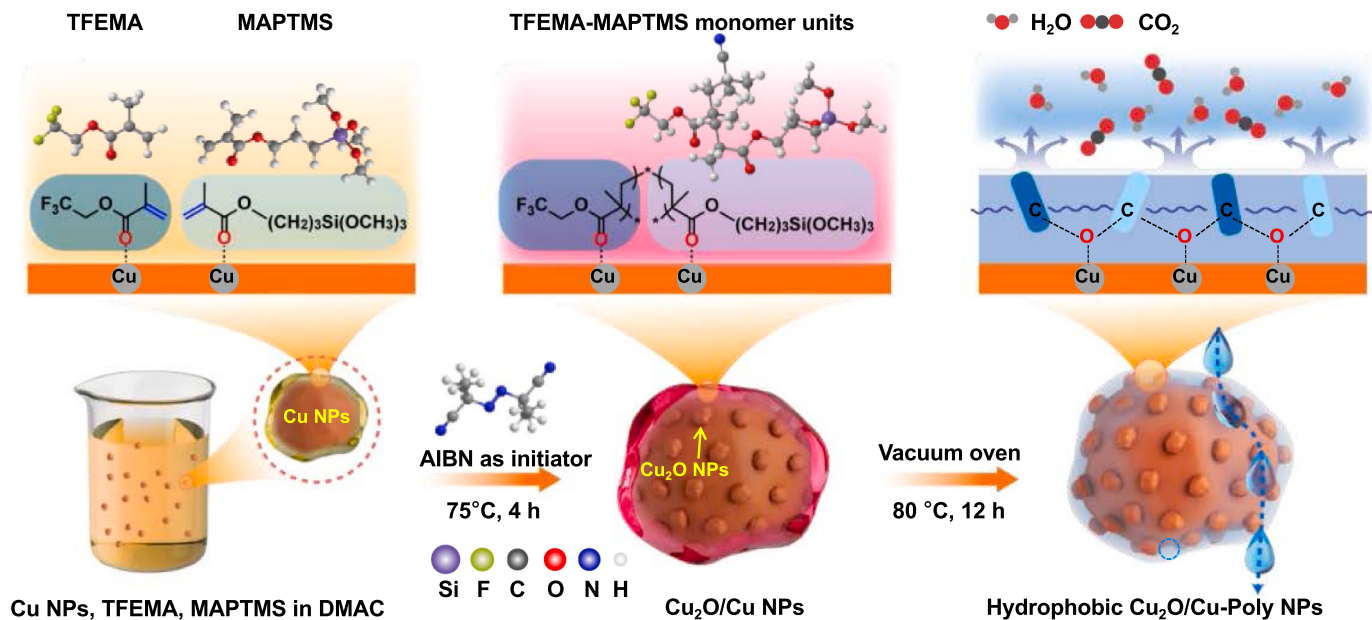
3.1. Catalysts preparation and characterizations

The Cu-poly was prepared by an in situ polymerization process [34]. Scheme 1 shows the procedures of the synthesis of Cu-poly catalysts. Briefly, Cu NPs, TFEMA with −CF₃ groups and MAPTMS with (CH₃O)₃Si− groups were mixed uniformly in DMAc by ultrasonication and then polymerized under the initiation of injecting AIBN. The polymer in Cu-poly-1 is composed of 1-(2,2,2-trifluoroethyl) 5-(3-(trimethoxysilyl)propyl) 2-(2-cyano-2-methylpropyl)-2,4-dimethylpentane dioate (abbreviated as TFEMA-MAPTMS, Fig. S3) monomers and is connected with Cu by covalent coordination effect originated from the unshared pair electrons of oxygen in carbonyl functional groups (Fig. S4). As shown in SEM and TEM images (Fig. S5), the bare Cu NPs possess an irregular morphology with aggregation of particles. While the morphology is largely maintained, the size of primary particles in Cu-poly-1 is much smaller than that of the pristine Cu NPs possibly due to the partial etching of Cu during polymerization process (Fig. 1a and Fig. S6). Besides, the polymer layer featuring a different monomer structure (Fig. S7) in Cu-poly-2 is much thicker with apparently higher ratio of carbon than that of Cu-poly-1 (Fig. S8 and Table S1), which indicates that the thickness and composition of the polymer could be regulated by adjusting the amount of reactants.

The Cu-poly-1 catalyst presents a polymer layer-wrapped polycrystalline structure containing Cu and Cu₂O, as evidenced by the HAADF-STEM images (Fig. 1b) and the concentric rings and bright discrete diffraction spots in the corresponding selected-area electron diffraction (SAED) patterns (Fig. 1c). Lattice fringes of an enlarged nanoparticle feature an interplanar distance of 0.24 nm (Fig. 1b inset), which is attributed to the (111) crystal plane of Cu₂O [44,45]. The coated polymer layer can be seen on different crystalline NPs in Cu-poly-1 (Fig. S9). Additionally, EDS mapping reveals uniform distribution of Cu, Si, F, C, and O after polymerization on Cu catalysts (Fig. 1d and Fig. S10). Furthermore, contact angle (CA) measurements indicate that the as-prepared Cu-poly-1/2 possess a significantly more hydrophobic surface than bare Cu due to the organic functional groups of the polymer (Fig. S11). The hydrophobicity of catalysts would suppress hydrogen evolution reaction (HER) while benefit to reduce the thickness of CO₂ gas diffusion layer and promote the mass transfer kinetics of CO₂ [46,47].

3.2. Phase structure and surface oxidation

The crystal phase structures of different catalysts were characterized by powder XRD. The bare Cu NPs and Cu-poly-1/2 samples show similar diffraction patterns, which can be readily assigned to a major phase of Cu and a minor phase of Cu₂O (Fig. 2a). As compared to Cu NPs, the relative intensity of Cu₂O (111) peak by normalizing to Cu (111) peaks is enhanced in Cu-poly-1/2 (Fig. S12), suggesting a higher ratio of Cu₂O due to the presence of carbonyl groups in polymerization. The presence of more oxidized Cu would result in a moderate affinity of *CO species that favors C–C coupling [48,49]. Anchoring polymers on the surface of Cu NPs can be evidenced from the FTIR spectroscopies (Fig. 2b). The strong absorption band at 1748 cm⁻¹ of Cu-poly-1/2 can be attributed to



Scheme 1. Schematic illustration for the preparation of hydrophobic polymer-coated Cu catalysts.

the $-\text{C=O}$ stretching vibration of the polymer and the vibration at 628 cm^{-1} corresponds to Cu-O bonds [34]. Also, the signal belong to carbonyl stretching can be identified in the spectra of MAPTMS and TFEMA (Fig. S13a).

For comparison, Cu NPs treated with single monomer (i.e., MAPTMS or TFEMA) were also prepared and characterized. As expected, Cu-MAPTMS and Cu-TFEMA catalysts show analogous FTIR spectra at 1748 cm^{-1} without $-\text{C=O}$ groups (Fig. S13b), suggesting that polymerization requires the addition of both MAPTMS and TFEMA molecules. Comparing the infrared data of monomers and Cu-poly-1/2 indicates that the coated polymeric layer is composed of TFEMA-MAPTMS copolymer. Additionally, the main peaks at 274 and 594 cm^{-1} in the Raman spectra could be attributed to the vibration of the Cu-O bonding (Fig. 2c). Collecting XRD, FTIR and Raman results confirms the increase of oxidized Cu species after polymerization on Cu NPs.

In survey XPS spectra, F is observed in Cu-poly-1/2 rather than bare Cu (Fig. S14), indicating the presence of $-\text{CF}_3$ functional groups in the polymer. High-resolution spectra of F 1s and Si 2s spectra reveal the formation of fluoric and silicious polymers (Fig. 2d). It is worth noting that the binding energy of Cu 2p_{3/2} in Cu-poly-1/2 (930.2 eV) is higher than that of bare Cu NPs (929.6 eV), as shown in Fig. 2e. Moreover, Cu Auger LMM spectra further show a higher binding energy of Cu in Cu-poly-1/2 than that of Cu NPs (Fig. S15). These results again indicate that more surface Cu was oxidized after the polymeric modification, which is favorable to the C-C coupling.

To characterize the texture of Cu and Cu-poly-1/2 catalysts, CO₂ and N₂ adsorption/desorption isotherm curves were recorded in an ice-water mixture and a liquid nitrogen bath, respectively. The higher amount of adsorbed gas in Cu-poly-1/2 than Cu clearly indicates enriched porous structures in the presence of polymers (Fig. 2f and Fig. S16). The determined specific surface area of Cu-poly-1/2 is also higher than that of Cu NPs (Fig. S16), which is due to the increased dispersity of Cu NPs induced by polymerization processing. Enhanced adsorption capacity would enrich the local concentration of CO₂ on the catalyst surface, contributing to increase of the total CO₂RR current density [29,30].

3.3. MEA cell measurements for CO₂RR

The products distribution on Cu, Cu-poly-1/2 were evaluated by adopting a MEA device with characteristics of the zero-gap, catholyte-

free and gas-direct electrolysis [50]. Fig. 3a shows the schematic configuration of assembled MEA cell. Gas diffusion electrode (GDE) is composed of a GDL and a catalysts layer (CL) of Cu or Cu-poly-1/2. As seen from the SEM images, the GDE features a thickness of $\sim 5.0 \mu\text{m}$, a porous structure and a rough surface (Fig. S17), which would favor the accessibility of electrolytes. Additionally, the three-dimensional contour plane profiles show that the catalyst is distributed uniformly in the electrode (Fig. S18). Intentionally, the area of GDE is slightly smaller than that of anode of NiFe LDH ($2.89 \text{ vs } 3.61 \text{ cm}^2$), aiming to achieve the maximal cathode utilization (Fig. S19). Flower-like NiFe LDH, with a superior oxygen evolution reaction (OER) activity compared with neat Ni foam in neutral electrolytes, is used as the counter electrode of CO₂RR cell (Fig. S20).

As shown in the linear sweep voltammetry (LSV) curves of Cu and Cu-poly-1/2, there is a slight decrease of total current density on polymer-modified Cu compared with bare Cu at the same potential, which is ascribed to the decreased electrochemically active surface area (Fig. S21 and S22). The composition of gaseous products was analyzed every 11 min by an online GC using chronopotentiometry from 300 to 550 mA cm^{-2} . For Cu-poly-1, the FE of H₂ fluctuates from 10.10 % at 400 mA cm^{-2} to 25.53 % at 550 mA cm^{-2} . Meanwhile, the FE of C₂H₄ increases from 28.59 % at 300 mA cm^{-2} to 41.80 % at 450 mA cm^{-2} (Fig. 3b). In comparison, the FE of H₂ for bare Cu NPs fluctuates from 20.93 % at 450 mA cm^{-2} to 32.70 % at 550 mA cm^{-2} , while the FE of C₂H₄ varies from 24.62 % at 300 mA cm^{-2} to 35.15 % at 500 mA cm^{-2} (Fig. 3c). Similarly, Cu-poly-2 shows the same trend as Cu-poly-1 (Fig. S23). These integral improvements of C₂H₄ production are mainly due to the enhanced coverage of *CO species, limited diffusion of H₂O and elevated interfacial concentration of CO₂ [51]. The polymer layer tends to prevent H₂O from flooding the surface of Cu-based catalysts due to the strong hydrophobicity of abundant silanic functional groups [34]. Meanwhile, the aerophilic characteristic would decrease the diffusion resistance of CO₂ and accelerate the CO₂ mass transfer dynamics [29]. In addition, the CO₂ enrichment near the surface of polymer modified Cu-based catalysts would promote the production of more *CO species, since the subsequent protonation reaction is limited due to the lack of sufficient proton source (H₂O) [52].

Besides gaseous products, liquid products generated from Cu NPs and Cu-poly-1/2 were collected at different current densities by employing the self-designed cold trap and analyzed by NMR. We also collected and analyzed the anolyte because of the possible crossover of

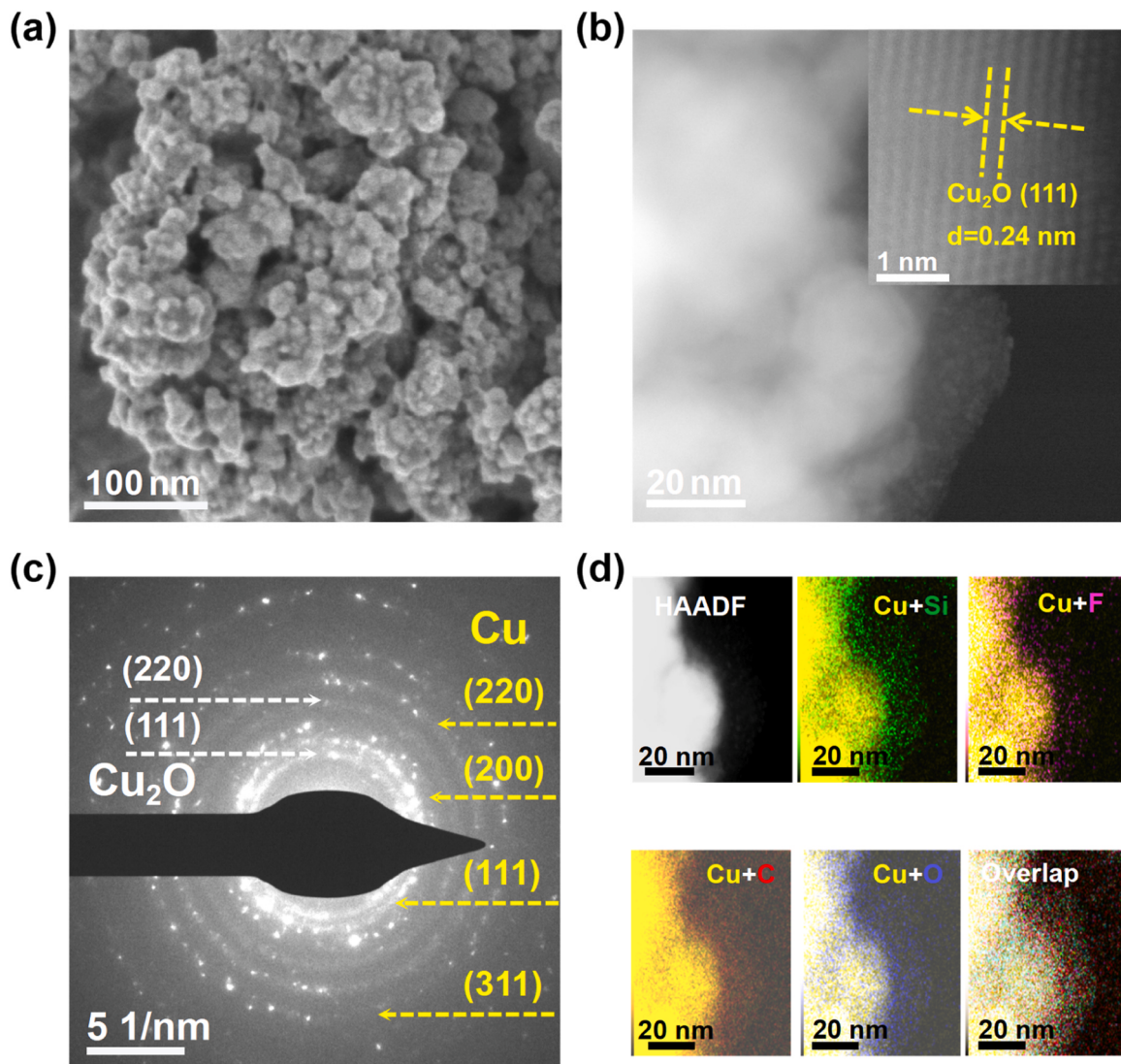


Fig. 1. (a) The SEM images, (b) the HAADF-STEM image, (c) SAED pattern, and (d) elemental mapping images of Cu-poly-1. Inset of (b) shows the corresponding HRTEM image of a nanoparticle. Color in (d): Cu yellow, Si green, F purple, C red, O blue.

the products driven by the electric field (Fig. S24). For all the three Cu-based electrodes, ethanol and propanol are the main liquid products. However, the FE of ethanol on Cu-poly-1/2 is higher than that on Cu NPs. At current density of 500 mA cm^{-2} , the FE_{C_2+} is 71.08 % and 64.22 % for Cu-poly-1 and Cu-poly-2, respectively, exceeding that of bare Cu (61.59 %) (Fig. 3d). It should be noted that the total FE of all gas and liquid products detected in each measurement is less than 100 % due to the loss of accumulated flow amount, which is caused by the frictional resistance of gas products flow across the pipes (Fig. S25) [53]. Furthermore, the difference in activity and selectivity between the two polymer-coated catalysts can be explained by two factors. Firstly, the content of oxidized Cu is lower in Cu-poly-1 than in Cu-poly-2, as revealed by XRD, Raman and CV curves (Fig. 2a,c and Fig. S26). The oxidation state of Cu exerts large effect on the selectivity of products in the CO₂RR on Cu-based electrocatalysts [54,55]. Secondly, the polymer layer in Cu-poly-1 is thinner than that of Cu-poly-2, which affects the local concentration of the reactants (CO₂ and H₂O) and thus the products distribution [56].

To evaluate the performance of polymer-coated catalysts, Table S2 compares the catalytic performances in terms of FE and current density of C₂₊ products for Cu-poly-1 and previous CO₂RR electrocatalysts using

the MEA cell. The products formation rates are also summarized in Table S3. Notably, the maximum value of FE and current density of C₂₊ products for Cu-poly-1 are 71.08 % and $-355.4 \text{ mA cm}^{-2}$, respectively, at the applied cell voltage of -3.98 V . Besides, the corresponding maximum formation rate of C₂₊ products is $1114.99 \mu\text{mol cm}^{-2} \text{ h}^{-1}$. These values are comparable to previously reported state-of-the-art CO₂RR catalysts. In addition to activity and selectivity, the stability of bare Cu and polymer-modified Cu NPs was investigated by SEM and TEM after CO₂ electrolysis. The nanoparticle morphology and porous texture are maintained in Cu, Cu-poly-1/2 catalysts (Fig. S27). The coated polymer layer and the oxidized Cu phase were also observed for both Cu-poly-1 and Cu-poly-2 catalysts (Fig. S28-30). Furthermore, the crystal planes of Cu (111) and Cu₂O (111) are visualized in tested bare Cu (Fig. S31). Then, the XPS spectra of Cu NPs and Cu-poly-1/2 catalysts after CO₂RR, operated at different current densities, were recorded to investigate the chemical states of Cu. The results indicate that both metallic Cu and oxidized Cu species exist in all three samples after CO₂RR (Fig. S32).

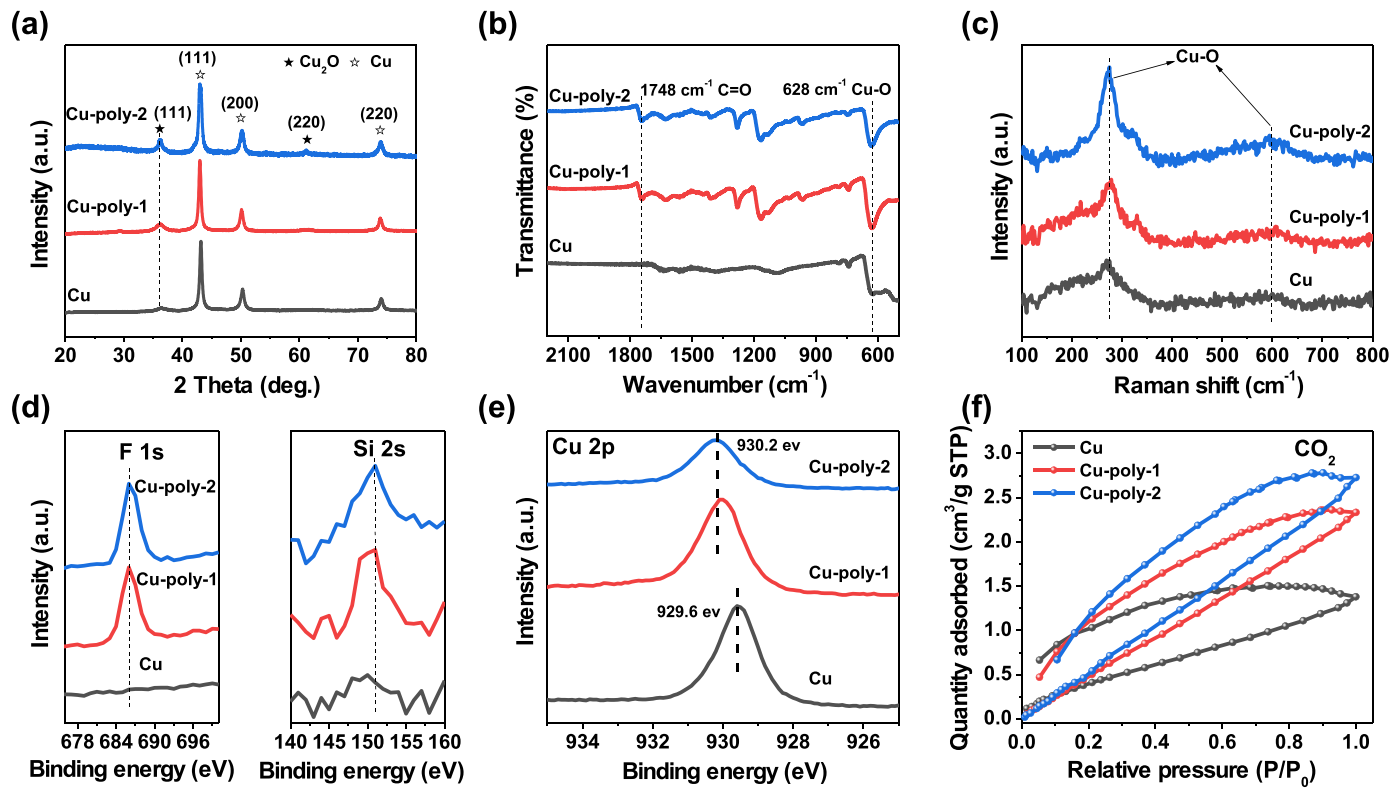


Fig. 2. (a) The XRD patterns, (b) FTIR spectra, (c) Raman spectra, (d) F 1s and Si 2s XPS spectra, (e) Cu 2p spectra, and (f) CO_2 adsorption/desorption curves of Cu NPs, Cu-poly-1, and Cu-poly-2.

3.4. In situ FTIR analysis

To gain a deep insight into the reaction mechanism, in situ ATR-SEIRAS spectroscopy was adopted to investigate the evolution of intermediates adsorbing on the surface of the catalysts. Fig. 4a and b show the real-time FTIR spectra of CO_2RR recorded on Cu and Cu-poly-1, respectively. An apparent band is detected from 2110 to 2080 cm^{-1} , which should be assigned to the stretching vibration of the linearly adsorbed $^*\text{CO}$ species, $\nu(\text{CO}_L)$ [57,58]. Meanwhile, the observed Stark effect of $\nu(\text{CO}_L)$ indicates that the applied potential would affect the vibration of $^*\text{CO}$ species during CO_2RR [59,60]. Particularly, the peak area of adsorbed CO_L is larger on Cu-poly-1 as compared to Cu NPs (Fig. 4a and b), suggesting increased coverage of $^*\text{CO}$ on polymer-modified Cu. As shown in Fig. 4c, Cu-poly-1 shows a lower wavenumber of $^*\text{CO}$ than that of Cu. Besides, the narrowing of the bandwidth of $\nu(\text{CO}_L)$ on Cu-poly-1 is also investigated, which indicates that the CO_L appeared to adsorb on Cu-poly-1 with a more ordered pattern and thus to provide a high possibility of C–C polymerization (Fig. S33) [51]. This spectroscopic analysis reveals the mechanism of the enhanced multicarbon products selectivity of Cu-poly-1 as compared to bare Cu NPs (Fig. 4d). In conclusion, Cu-poly-1 presents a relative high coverage of $^*\text{CO}$ as compared to bare Cu, which is beneficial to the dimerization of $^*\text{CO}$ and further to generate C_{2+} products [61].

3.5. DFT study on reaction mechanism

DFT calculations were further conducted to reveal the effect of polymer on the adsorption energy of $^*\text{CO}$ and formation energy of $^*\text{COCOH}$ intermediates over Cu NPs and polymer modified Cu (Cu-poly). The optimized configurations of adsorbed $^*\text{CO}$ show that the bond length of Cu-CO on Cu-poly slightly increases as compared to Cu NPs (1.858 vs 1.848 Å), which is caused by the electrostatic interaction and the weak steric hindrance of the polymers (Fig. 5a, Fig. S34 and S35). In

addition, the adsorption energy of $^*\text{CO}$ on Cu NPs is more negative as compared to Cu-poly (-1.44 vs. -1.03 eV, Fig. 5b), indicating that the $^*\text{CO}$ species prefer to stably adsorb on Cu sites and are difficult to release, which is more favorable to the subsequent hydrogenation (forming C_1 products) instead of C–C polymerization to generate C_{2+} species [54,62]. Furthermore, the optimized models of $^*\text{COCOH}$ intermediates adsorbing on Cu NPs and Cu-poly suggest the formation of hydrogen bonds between the $-\text{CF}_3$ functional groups and $^*\text{COCOH}$ species (Fig. 5c, Fig. S36 and S37) [63]. Thus, the formation energy of $^*\text{COCOH}$ on Cu-poly is lower than that of Cu NPs (2.27 vs. 2.37 eV), which indicates that the polymer modified Cu is favorable to form C_{2+} species rather than C_1 hydrocarbons (Fig. 5b). Fig. 5d shows the proposed reaction pathway for CO_2RR to C_{2+} products on Cu-poly catalysts. Consequently, Cu-poly-1 with sufficient $^*\text{CO}$ coverage and relatively low $^*\text{COCOH}$ formation energy prefers to enhance the C–C coupling and thus the formation of C_{2+} products.

4. Conclusion

In summary, we demonstrated a free radical thermal polymerization method for the facile synthesis of polymers coating Cu catalysts. The modified Cu NPs present enhanced selectivity and current density of C_{2+} products in CO_2RR as compared to bare Cu NPs. Combining in situ infrared spectroscopic analysis and DFT calculations, the improved catalytic performances could be attributed to the enhanced coverage of $^*\text{CO}$ and decreased formation energy of $^*\text{COCOH}$ intermediates. Consequently, Cu-poly-1 delivers an excellent CO_2RR performance of C_{2+} products with a Faradaic efficiency of 71.08 % at a cell voltage of -3.98 V using MEA electrolyzer. This work offers a novel strategy for fabricating polymers modified Cu-based catalyst for CO_2 electrochemical reduction and provides a promising pathway to tuning the selectivity of C_{2+} products through the regulation of electrochemical microenvironment.

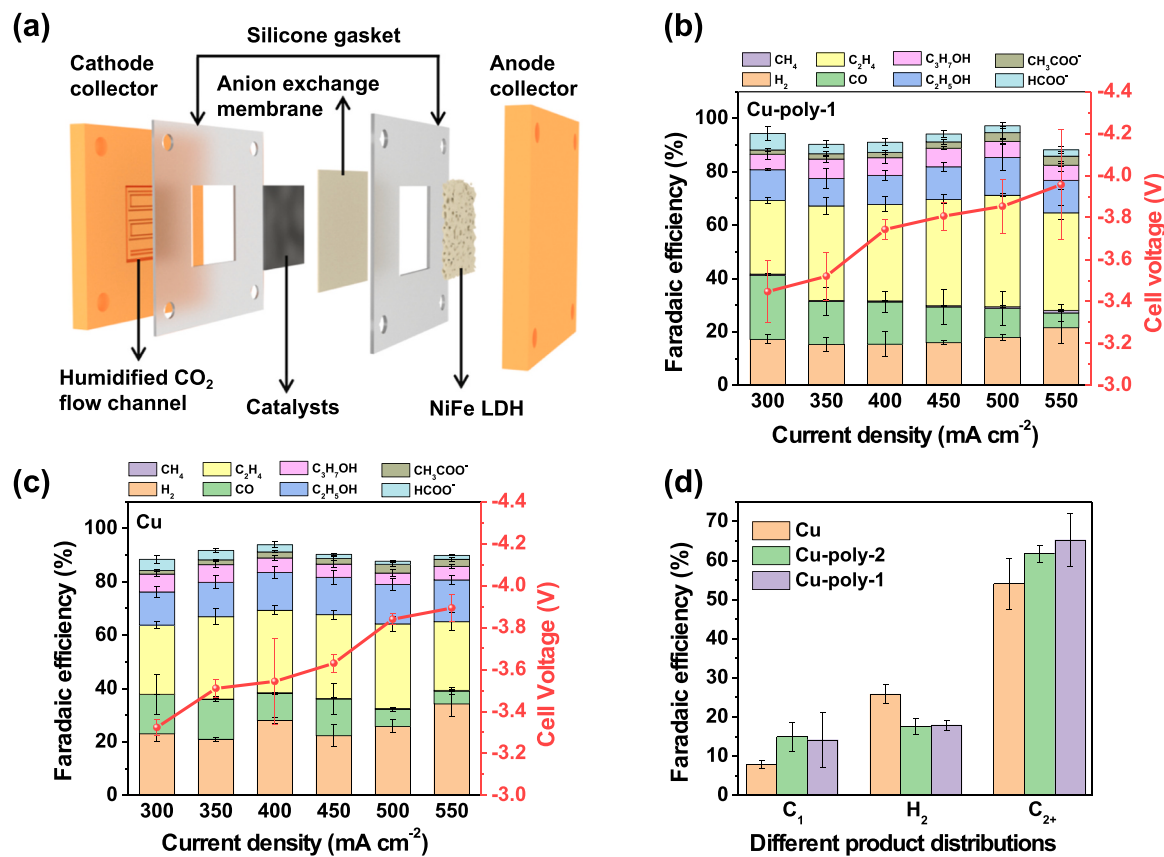


Fig. 3. (a) Schematic illustration of the MEA cell configuration, using Cu-poly-1/2 and NiFe LDH as cathode and anode catalyst separately in contact with the AEM. (b) The FE and cell voltage of (b) Cu-poly-1 and (c) Cu with respect to the applied total current density. (d) FE of H_2 , C_1 , and C_{2+} products from the CO_2 RR on Cu (faint yellow), Cu-poly-1 (pale green), and Cu-poly-2 (light purple) at current density of 500 mA cm^{-2} .

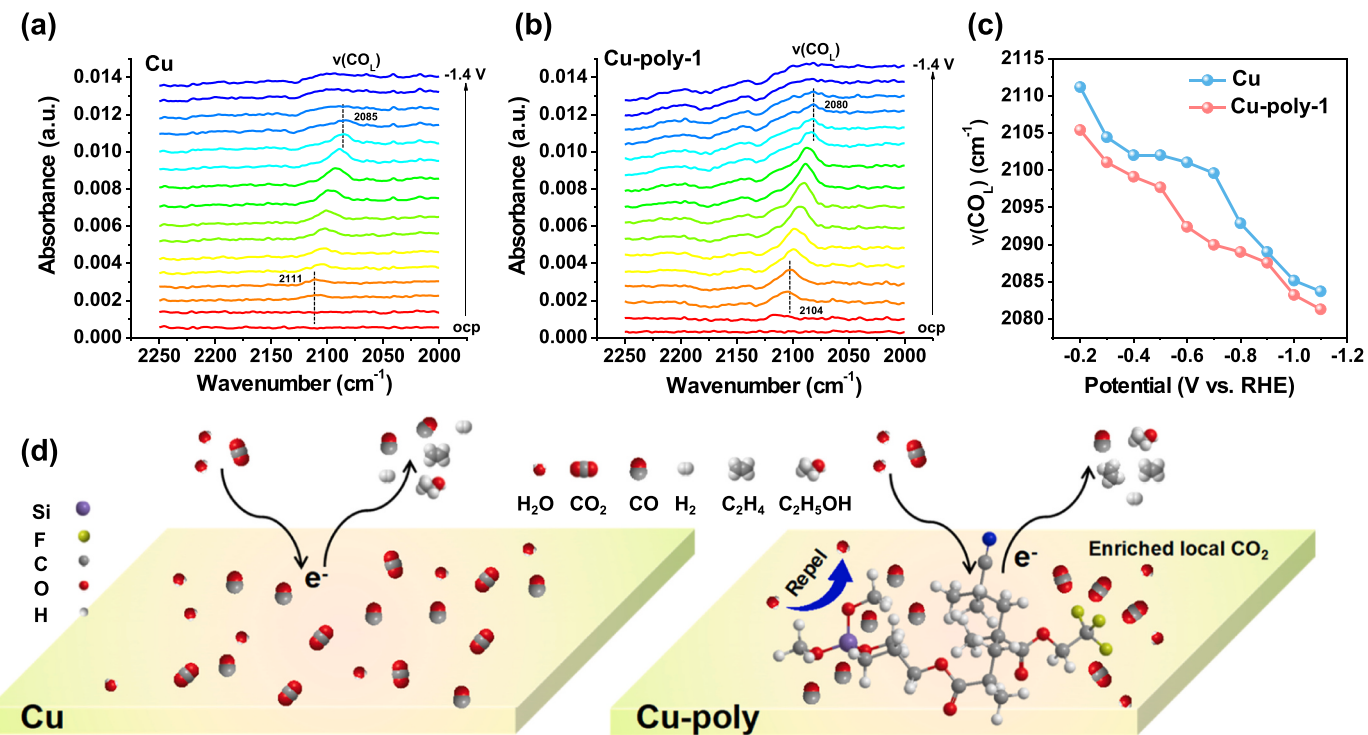


Fig. 4. In situ ATR-SEIRAS spectra of CO_2 RR on the (a) Cu NPs and (b) Cu-poly-1 electrodes in CO_2 -saturated 1 M KHO_3 . (c) Stark effects of the linearly adsorbed CO (CO_L) on Cu NPs and Cu-poly-1 electrodes. (d) Schematic illustrations of the CO_2 RR mechanism on the Cu NPs and Cu-poly electrodes.

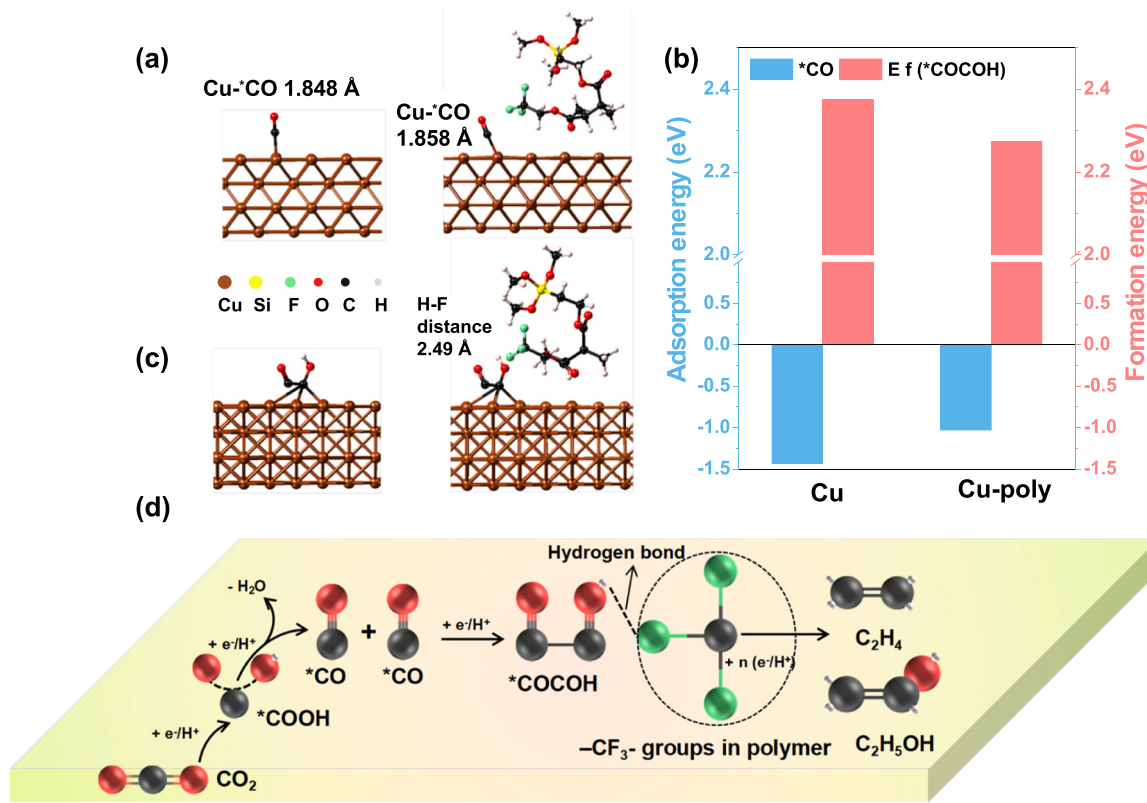


Fig. 5. Optimized adsorption configuration of (a) *CO and (c) *COCOH on Cu and Cu-poly. (b) The adsorption energy of *CO and formation energy of *COCOH on Cu and Cu-poly. (d) Proposed reaction pathway for CO₂RR to C₂₊ products on Cu-poly.

CRediT authorship contribution statement

Tete Zhao: conceptualization, experiments, visualization, writing-original draft. **Xupeng Zong:** DFT calculations and formal analysis. **Jiuding Liu and Jiale Chen:** software and visualization. **Keqiang Xu:** formal analysis. **Xiao Wang, Jiexi Chen and Wutong Yang:** experiments and formal analysis. **Meng Yu:** writing-review & editing, formal analysis. **Fangyi Cheng:** conceptualization, writing-review & editing, supervision.

Declaration of Competing Interest

The authors declare that they have no known competing financial interests or personal relationships that could have appeared to influence the work reported in this paper.

Data availability

Data will be made available on request.

Acknowledgments

This work was financially supported by NSFC (22121005, 21925503, 21835504, and 22102076), the MOST (2022YFA1504001), and the Fundamental Research Funds for the Central Universities. Computations were carried out on TianHe-1(A) at National Supercomputer Center in Tianjin. We thank Prof. Huan Wang at Nankai University for her suggestion on MEA schematic illustration.

Appendix A. Supporting information

Supplementary data associated with this article can be found in the online version at [doi:10.1016/j.apcatb.2023.123281](https://doi.org/10.1016/j.apcatb.2023.123281).

References

- [1] Y.Y. Birdja, E. Pérez-Gallent, M.C. Figueiredo, A.J. Göttle, F. Calle-Vallejo, M.T. M. Koper, Advances and challenges in understanding the electrocatalytic conversion of carbon dioxide to fuels, *Nat. Energy* 4 (2019) 732–745, <https://doi.org/10.1038/s41560-019-0450-y>.
- [2] M.B. Ross, P. De Luna, Y. Li, C.T. Dinh, D. Kim, P. Yang, E.H. Sargent, Designing materials for electrochemical carbon dioxide recycling, *Nat. Catal.* 2 (2019) 648–658, <https://doi.org/10.1038/s41929-019-0306-7>.
- [3] Y. Hori, A. Murata, R. Takahashi, Formation of hydrocarbons in the electrochemical reduction of carbon dioxide at a copper electrode in aqueous solution, *J. Chem. Soc. Faraday Trans.* 185 (1989) 2309–2326, <https://doi.org/10.1039/f19898502309>.
- [4] K. Wang, D. Liu, L. Liu, J. Liu, X. Hu, P. Li, M. Li, A.S. Vasenko, C. Xiao, S. Ding, Tuning the local electronic structure of oxygen vacancies over copper-doped zinc oxide for efficient CO₂ electroreduction, *eScience* 2 (2022) 518–528, <https://doi.org/10.1016/j.esci.2022.08.002>.
- [5] J. Albo, D. Vallejo, G. Beobide, O. Castillo, P. Castano, A. Irabien, Copper-based metal-organic porous materials for CO₂ electrocatalytic reduction to alcohols, *ChemSusChem* 10 (2017) 1100–1109, <https://doi.org/10.1002/cssc.20160093>.
- [6] I. Merino-García, J. Albo, J. Solla-Gullón, V. Montiel, A. Irabien, Cu oxide/ZnO-based surfaces for a selective ethylene production from gas-phase CO₂ electroconversion, *J. CO₂ Util.* 31 (2019) 135–142, <https://doi.org/10.1016/j.jcou.2019.03.002>.
- [7] W. Li, L. Li, Q. Xia, S. Hong, L. Wang, Z. Yao, T.-S. Wu, Y.-L. Soo, H. Zhang, T.W. B. Lo, A.W. Robertson, Q. Liu, L. Hao, Z. Sun, Lowering C–C coupling barriers for efficient electrochemical CO₂ reduction to C₂H₄ by jointly engineering single Bi atoms and oxygen vacancies on CuO, *Appl. Catal. B: Environ.* 318 (2022), 121823, <https://doi.org/10.1016/j.apcatb.2022.121823>.
- [8] A. Dutta, M. Rahaman, N.C. Luedi, M. Mohos, P. Broekmann, Morphology matters: tuning the product distribution of CO₂ electroreduction on oxide-derived Cu foam catalysts, *ACS Catal.* 6 (2016) 3804–3814, <https://doi.org/10.1021/acscatal.6b00770>.
- [9] H. Li, H. Zhou, Y. Zhou, J. Hu, M. Miyauchi, J. Fu, M. Liu, Electric-field promoted C–C coupling over Cu nanoneedles for CO₂ electroreduction to C₂ products, *Chin. J. Catal.* 43 (2022) 519–525, [https://doi.org/10.1016/s1872-2067\(21\)63866-4](https://doi.org/10.1016/s1872-2067(21)63866-4).
- [10] D. Zhong, Z.-J. Zhao, Q. Zhao, D. Cheng, B. Liu, G. Zhang, W. Deng, H. Dong, L. Zhang, J. Li, J. Li, J. Gong, Coupling of Cu (100) and (110) facets promotes carbon dioxide conversion to hydrocarbons and alcohols, *Angew. Chem. Int. Ed.* 60 (2021) 4879–4885, <https://doi.org/10.1002/anie.202015159>.
- [11] M. Philip, A.R. Woldu, M.B. Akbar, H. Louis, H. Cong, A facile synthesis of Cu catalysts with multiple high-index facets for the suppression of competing H₂

- evolution during electrocatalytic CO₂ reduction, *Nanoscale* 13 (2021) 3042–3048, <https://doi.org/10.1039/d0nr07286a>.
- [12] Y. Fu, Q. Xie, L. Wu, J. Luo, Crystal facet effect induced by different pretreatment of Cu₂O nanowire electrode for enhanced electrochemical CO₂ reduction to C₂₊ products, *Chin. J. Catal.* 43 (2022) 1066–1073, [https://doi.org/10.1016/s1872-2067\(21\)63981-5](https://doi.org/10.1016/s1872-2067(21)63981-5).
- [13] Z. Lyu, S. Zhu, M. Xie, Y. Zhang, Z. Chen, R. Chen, M. Tian, M. Chi, M. Shao, Y. Xia, Controlling the surface oxidation of Cu nanowires improves their catalytic selectivity and stability toward C₂₊ products in CO₂ reduction, *Angew. Chem. Int. Ed.* 60 (2021) 1909–1915, <https://doi.org/10.1002/anie.202011956>.
- [14] X. Lv, Q. Liu, J. Wang, X. Wu, X. Li, Y. Yang, J. Yan, A. Wu, H.B. Wu, Grain refining enables mixed Cu⁺/Cu⁰ states for CO₂ electroreduction to C₂₊ products at high current density, *Appl. Catal. B: Environ.* 324 (2023), 122272, <https://doi.org/10.1016/j.apcatb.2022.122272>.
- [15] R. Reske, H. Mistry, F. Behafarid, B. Roldan Cuanya, P. Strasser, Particle size effects in the catalytic electroreduction of CO₂ on Cu nanoparticles, *J. Am. Chem. Soc.* 136 (2014) 6978–6986, <https://doi.org/10.1021/ja500328k>.
- [16] I. Merino-Garcia, J. Albo, A. Irabien, Tailoring gas-phase CO₂ electroreduction selectivity to hydrocarbons at Cu nanoparticles, *Nanotechnology* 29 (2018), 014001, <https://doi.org/10.1088/1361-6528/aa994e>.
- [17] H. Rabiee, L. Ge, X. Zhang, S. Hu, M. Li, S. Smart, Z. Zhu, H. Wang, Z. Yuan, Stand-alone asymmetric hollow fiber gas-diffusion electrodes with distinguished bronze phases for high-efficiency CO₂ electrochemical reduction, *Appl. Catal. B: Environ.* 298 (2021), 120538, <https://doi.org/10.1016/j.apcatb.2021.120538>.
- [18] T. Zhao, J. Li, J. Liu, F. Liu, K. Xu, M. Yu, W. Xu, F. Cheng, Tailoring the catalytic microenvironment of Cu₂O with SiO₂ to enhance C₂₊ product selectivity in CO₂ electroreduction, *ACS Catal.* 13 (2023) 4444–4453, <https://doi.org/10.1021/acscatal.3c00056>.
- [19] K. Xu, J. Li, F. Liu, W. Xu, T. Zhao, F. Cheng, Steering CO₂ electroreduction selectivity towards CH₄ and C₂H₄ on a tannic acid-modified Cu electrode, *Mater. Chem. Front.* 7 (2023) 1395–1402, <https://doi.org/10.1039/d2qm01259f>.
- [20] D. Wang, J. Mao, C. Zhang, J. Zhang, J. Li, Y. Zhang, Y. Zhi, Modulating microenvironments to enhance CO₂ electroreduction performance, *eScience* 3 (2023), 100119, <https://doi.org/10.1016/j.esci.2023.100119>.
- [21] J. Gong, J. Li, C. Liu, F. Wei, J. Yin, W. Li, L. Xiao, G. Wang, J. Lu, L. Zhuang, Guanine-regulated proton transfer enhances CO₂-to-CH₄ selectivity over copper electrode, *Chin. J. Catal.* 43 (2022) 3101–3106, [https://doi.org/10.1016/s1872-2067\(22\)64113-5](https://doi.org/10.1016/s1872-2067(22)64113-5).
- [22] R.F. Weiss, Carbon dioxide in water and seawater: the solubility of a non-ideal gas, *Mar. Chem.* 2 (1974) 203–215, [https://doi.org/10.1016/0304-4203\(74\)90015-2](https://doi.org/10.1016/0304-4203(74)90015-2).
- [23] T. Burdyny, W.A. Smith, CO₂ reduction on gas-diffusion electrodes and why catalytic performance must be assessed at commercially-relevant conditions, *Energy Environ. Sci.* 12 (2019) 1442–1453, <https://doi.org/10.1039/c8ee03134g>.
- [24] L. Ge, H. Rabiee, M. Li, S. Subramanian, Y. Zheng, J.H. Lee, T. Burdyny, H. Wang, Electrochemical CO₂ reduction in membrane-electrode assemblies, *Chem* 8 (2022) 663–692, <https://doi.org/10.1016/j.chempr.2021.12.002>.
- [25] W. Lee, Y.E. Kim, M.H. Youn, S.K. Jeong, K.T. Park, Catholyte-free electrocatalytic CO₂ reduction to formate, *Angew. Chem. Int. Ed.* 57 (2018) 6883–6887, <https://doi.org/10.1002/anie.201803501>.
- [26] Z. Liu, H. Yang, R. Kutz, R.I. Masel, CO₂ electrolysis to CO and O₂ at high selectivity, stability and efficiency using sustainain membranes, *J. Electrochem. Soc.* 165 (2018), J3371, <https://doi.org/10.1149/2.0501815jes>.
- [27] D.G. Wheeler, B.A.W. Mowbray, A. Reyes, F. Habibzadeh, J. He, C.P. Berlinguet, Quantification of water transport in a CO₂ electrolyzer, *Energy Environ. Sci.* 13 (2020) 5126–5134, <https://doi.org/10.1039/d0ee02219e>.
- [28] W. Choi, S. Park, W. Jung, D.H. Won, J. Na, Y.J. Hwang, Origin of hydrogen incorporated into ethylene during electrochemical CO₂ reduction in membrane electrode assembly, *ACS Energy Lett.* 7 (2022) 939–945, <https://doi.org/10.1021/acsenergylett.1c02658>.
- [29] Z. Xing, L. Hu, D.S. Ripatti, X. Hu, X. Feng, Enhancing carbon dioxide gas-diffusion electrolysis by creating a hydrophobic catalyst microenvironment, *Nat. Commun.* 12 (2021) 136, <https://doi.org/10.1038/s41467-020-20397-5>.
- [30] H.-Q. Liang, S. Zhao, X.-M. Hu, M. Ceccato, T. Skrydstrup, K. Daasbjerg, Hydrophobic copper interfaces boost electroreduction of carbon dioxide to ethylene in water, *ACS Catal.* 11 (2021) 958–966, <https://doi.org/10.1021/acscatal.0c03766>.
- [31] Y. Wu, L. Charlesworth, I. Maglaya, M.N. Idros, M. Li, T. Burdyny, G. Wang, T. E. Rufford, Mitigating electrolyte flooding for electrochemical CO₂ reduction via infiltration of hydrophobic particles in a gas diffusion layer, *ACS Energy Lett.* 7 (2022) 2884–2892, <https://doi.org/10.1021/acsenergylett.2c01555>.
- [32] D. Wakerley, S. Lamaison, F. Ozanam, N. Menguy, D. Mercier, P. Marcus, M. Fontecave, V. Mougel, Bio-inspired hydrophobicity promotes CO₂ reduction on a Cu surface, *Nat. Mater.* 18 (2019) 1222–1227, <https://doi.org/10.1038/s41563-019-0445-x>.
- [33] L. Wang, P. Liu, Y. Xu, Y. Zhao, N. Xue, X. Guo, L. Peng, Y. Zhu, M. Ding, Q. Wang, W. Ding, Enhanced catalytic activity and stability of bismuth nanosheets decorated by 3-aminopropyltriethoxysilane for efficient electrochemical reduction of CO₂, *Appl. Catal. B: Environ.* 298 (2021), 120602, <https://doi.org/10.1016/j.apcatb.2021.120602>.
- [34] M. Ding, H.-L. Jiang, Improving water stability of metal–organic frameworks by a general surface hydrophobic polymerization, *CCS Chem.* 3 (2020) 2740–2748, <https://doi.org/10.31635/ccschem.020.202000515>.
- [35] H. Yang, C. Wang, Y. Zhang, Q. Wang, Green synthesis of NiFe LDH/Ni foam at room temperature for highly efficient electrocatalytic oxygen evolution reaction, *Sci. China Mater.* 62 (2018) 681–689, <https://doi.org/10.1007/s40843-018-9356-1>.
- [36] C.M. Gabardo, C.P. O'Brien, J.P. Edwards, C. McCallum, Y. Xu, C.-T. Dinh, J. Li, E. H. Sargent, D. Sinton, Continuous carbon dioxide electroreduction to concentrated multi-carbon products using a membrane electrode assembly, *Joule* 3 (2019) 2777–2791, <https://doi.org/10.1016/j.joule.2019.07.021>.
- [37] R. Chen, H.Y. Su, D. Liu, R. Huang, X. Meng, X. Cui, Z.Q. Tian, D.H. Zhang, D. Deng, Highly selective production of ethylene by the electroreduction of carbon monoxide, *Angew. Chem. Int. Ed.* 59 (2020) 154–160, <https://doi.org/10.1002/anie.201910662>.
- [38] I.M. Garcia, J. Albo, A. Irabien, Productivity and selectivity of gas-phase CO₂ electroreduction to methane at copper nanoparticle based electrodes, *Energy Technol.* 5 (2017) 922–928, <https://doi.org/10.1002/ente.201600616>.
- [39] W. Ma, S. Xie, X.G. Zhang, F. Sun, J. Kang, Z. Jiang, Q. Zhang, D.Y. Wu, Y. Wang, Promoting electrocatalytic CO₂ reduction to formate via sulfur-boosting water activation on indium surfaces, *Nat. Commun.* 10 (2019) 892, <https://doi.org/10.1038/s41467-019-108805-x>.
- [40] X. Xie, X. Zhang, M. Xie, L. Xiong, H. Sun, Y. Lu, Q. Mu, M.H. Rummeli, J. Xu, S. Li, J. Zhong, Z. Deng, B. Ma, T. Cheng, W.A. Goddard 3rd, Y. Peng, Au-activated N motifs in non-coherent cupric porphyrin metal organic frameworks for promoting and stabilizing ethylene production, *Nat. Commun.* 13 (2022) 63, <https://doi.org/10.1038/s41467-021-2776-6>.
- [41] G. Kresse, J. Furthmüller, Efficient iterative schemes for ab initio total-energy calculations using a plane-wave basis set, *Phys. Rev. B* 54 (1996) 11169–11186, <https://doi.org/10.1103/physrevb.54.11169>.
- [42] K. Burke, M. Ernzerhof, J.P. Perdew, The adiabatic connection method: a non-empirical hybrid, *Chem. Phys. Lett.* 265 (1997) 115–120, [https://doi.org/10.1016/s0009-2614\(96\)01373-5](https://doi.org/10.1016/s0009-2614(96)01373-5).
- [43] L. Li, Z.J. Zhao, G. Zhang, D. Cheng, X. Chang, X. Yuan, T. Wang, J. Gong, Neural network accelerated investigation of the dynamic structure-performance relations of electrochemical CO₂ reduction over SnO_x surfaces, *Research* 6 (2023) 0067, <https://doi.org/10.34133/research.0067>.
- [44] Y. Yang, S. Louisia, S. Yu, J. Jin, I. Roh, C. Chen, M.V. Fonseca Guzman, J. Feijoo, P.C. Chen, H. Wang, C.J. Pollock, X. Huang, Y.T. Shao, C. Wang, D.A. Muller, H. Abruna, P. Yang, Operando studies reveal active Cu nanograins for CO₂ electroreduction, *Nature* 614 (2023) 262–269, <https://doi.org/10.1038/s41586-022-05540-0>.
- [45] B. Deng, M. Huang, K. Li, X. Zhao, Q. Geng, S. Chen, H. Xie, X. Dong, H. Wang, F. Dong, Crystal plane is not the key factor for CO₂-to-methane electrosynthesis on reconstructed Cu₂O microparticles, *Angew. Chem. Int. Ed.* 61 (2021), e202114080, <https://doi.org/10.1002/anie.202114080>.
- [46] H. Rabiee, L. Ge, J. Zhao, X. Zhang, M. Li, S. Smart, T.E. Rufford, Z. Zhu, H. Wang, Z. Yuan, Regulating the reaction zone of electrochemical CO₂ reduction on gas-diffusion electrodes by distinctive hydrophilic-hydrophobic catalyst layers, *Appl. Catal. B: Environ.* 310 (2022), 121362, <https://doi.org/10.1016/j.apcatb.2022.121362>.
- [47] Y. Zhang, R. Zhang, F. Chen, F. Zhang, Y. Liu, X. Hao, H. Jin, X. Zhang, Z. Lu, H. Dong, F. Lu, W. Wang, H. Liu, H. Liu, Y. Cheng, Mass-transfer-enhanced hydrophobic Bi microsheets for highly efficient electroreduction of CO₂ to pure formate in a wide potential window, *Appl. Catal. B: Environ.* 322 (2023), 122127, <https://doi.org/10.1016/j.apcatb.2022.122127>.
- [48] J. Zhang, Y. Wang, Z. Li, S. Xia, R. Cai, L. Ma, T. Zhang, J. Ackley, S. Yang, Y. Wu, J. Wu, Grain boundary-derived Cu⁺/Cu⁰ interfaces in CuO nanosheets for low overpotential carbon dioxide electroreduction to ethylene, *Adv. Sci.* 9 (2022), 2200454, <https://doi.org/10.1002/adv.202200454>.
- [49] H. Mistry, A.S. Varela, C.S. Bonifacio, I. Zegkinoglou, I. Sinev, Y.W. Choi, K. Kisslinger, E.A. Stach, J.C. Yang, P. Strasser, B.R. Cuanya, Highly selective plasma-activated copper catalysts for carbon dioxide reduction to ethylene, *Nat. Commun.* 7 (2016), 12123, <https://doi.org/10.1038/ncomms12123>.
- [50] E.W. Lees, B.A.W. Mowbray, F.G.L. Parlane, C.P. Berlinguet, Gas diffusion electrodes and membranes for CO₂ reduction electrolyzers, *Nat. Rev. Mater.* 7 (2021) 55–64, <https://doi.org/10.1038/s41578-021-00356-2>.
- [51] X. Wei, Z. Yin, K. Lyu, Z. Li, J. Gong, G. Wang, L. Xiao, J. Lu, L. Zhuang, Highly selective reduction of CO₂ to C₂₊ hydrocarbons at copper/polyaniline interfaces, *ACS Catal.* 10 (2020) 4103–4111, <https://doi.org/10.1021/acscatal.0c00049>.
- [52] T.K. Todorova, M.W. Schreiber, M. Fontecave, Mechanistic understanding of CO₂ reduction reaction (CO₂RR) toward multicarbon products by heterogeneous copper-based catalysts, *ACS Catal.* 10 (2019) 1754–1768, <https://doi.org/10.1021/acscatal.9b04746>.
- [53] H. Lu, R. Ruan, X. Guo, H. Liu, Modeling study on the pressure drop and characteristic velocity of the pneumatic logistics transmission system, *Ind. Eng. Chem. Res.* 62 (2023) 6301–6310, <https://doi.org/10.1021/acs.iecr.3c00159>.
- [54] X. Yuan, S. Chen, D. Cheng, Z. Li, W. Zhu, D. Zhong, Z.J. Zhao, J. Li, T. Wang, J. Gong, Controllable Cu⁰-Cu⁺ sites for electrocatalytic reduction of carbon dioxide, *Angew. Chem. Int. Ed.* 60 (2021) 15344–15347, <https://doi.org/10.1002/anie.202105118>.
- [55] S.Y. Lee, H. Jung, N.-K. Kim, H.-S. Oh, B.K. Min, Y.J. Hwang, Mixed copper states in anodized Cu electrocatalyst for stable and selective ethylene production from CO₂ reduction, *J. Am. Chem. Soc.* 140 (2018) 8681–8689, <https://doi.org/10.1021/jacs.8b02173>.
- [56] J. Wang, T. Cheng, A.Q. Fenwick, T.N. Baroud, A. Rosas-Hernandez, J.H. Ko, Q. Gan, W.A. Goddard III, R.H. Grubbs, Selective CO₂ electrochemical reduction enabled by a tricomponent copolymer modifier on a copper surface, *J. Am. Chem. Soc.* 143 (2021) 2857–2865, <https://doi.org/10.1021/jacs.0c12478>.
- [57] Z. Li, Y. Yang, Z. Yin, X. Wei, H. Peng, K. Lyu, F. Wei, L. Xiao, G. Wang, H. D. Abruna, J. Lu, L. Zhuang, Interface-enhanced catalytic selectivity on the C₂ products of CO₂ electroreduction, *ACS Catal.* 11 (2021) 2473–2482, <https://doi.org/10.1021/acscatal.0c03846>.

- [58] H. Li, K. Jiang, S.-Z. Zou, W.-B. Cai, Fundamental aspects in CO₂ electroreduction reaction and solutions from in situ vibrational spectroscopies, *Chin. J. Catal.* 43 (2022) 2772–2791, [https://doi.org/10.1016/S1872-2067\(22\)64095-6](https://doi.org/10.1016/S1872-2067(22)64095-6).
- [59] J. Heyes, M. Dunwell, B. Xu, CO₂ reduction on Cu at low overpotentials with surface-enhanced in situ spectroscopy, *J. Phys. Chem. C* 120 (2016) 17334–17341, <https://doi.org/10.1021/acs.jpcc.6b03065>.
- [60] S. Zhu, B. Jiang, W.B. Cai, M. Shao, Direct observation on reaction intermediates and the role of bicarbonate anions in CO₂ electrochemical reduction reaction on Cu surfaces, *J. Am. Chem. Soc.* 139 (2017) 15664–15667, <https://doi.org/10.1021/jacs.7b10462>.
- [61] S. Ahn, K. Klyukin, R.J. Wakeham, J.A. Rudd, A.R. Lewis, S. Alexander, F. Carla, V. Alexandrov, E. Andreoli, Poly-amide modified copper foam electrodes for enhanced electrochemical reduction of carbon dioxide, *ACS Catal.* 8 (2018) 4132–4142, <https://doi.org/10.1021/acscatal.7b04347>.
- [62] X. Zhou, J. Shan, L. Chen, B.Y. Xia, T. Ling, J. Duan, Y. Jiao, Y. Zheng, S.Z. Qiao, Stabilizing Cu²⁺ ions by solid solutions to promote CO₂ electroreduction to methane, *J. Am. Chem. Soc.* 144 (2022) 2079–2084, <https://doi.org/10.1021/jacs.1c12212>.
- [63] R. Wang, M. Yao, M. Yang, J. Zhu, J. Chen, Z. Niu, Synergetic modulation on ionic association and solvation structure by electron-withdrawing effect for aqueous zinc-ion batteries, *Proc. Natl. Acad. Sci. USA* 120 (2023), e2221980120, <https://doi.org/10.1073/pnas.2221980120>.